Proceedings of the Twenty-ninth (2019) International Ocean and Polar Engineering Conference **www.isope.org**
Honolulu, Hawaii, USA, June 16-21, 2019

ISBN 978-1 880653 85-2; ISSN 1098-6189

Infragravity-wave Dominance at Sea-Dikes fronted by Very and Extremely Shallow Foreshores

Christopher H. Lashley [1], Jeremy D. Bricker [1], Jentsje van der Meer [2], Corrado Altomare [3], Tomohiro Suzuki [4]

[1] Hydraulic Engineering, Delft University of Technology, Delft, the Netherlands

[2] Water Science & Engineering, IHE-Delft, Delft, the Netherlands

[3] Civil Engineering, Ghent University, Ghent, Belgium

[4] Flanders Hydraulics Research, Antwerp, Belgium

ABSTRACT

While the significance of infragravity waves (IG) in many—often-hazardous—nearshore processes is widely-recognized, many of the empirical and numerical models used in dike safety assessments do not (directly) consider their contribution. Here, we combine physical and numerical modelling to better understand the factors that contribute to the dominance of IG waves over higher-frequency waves at the dike toe. Findings show that IG-wave dominance increases as the ratio of local water depth to offshore significant wave height decreases. Therefore, it is critical that any tool used to assess the safety of dikes fronted by very and extremely shallow foreshores accurately describe IG-wave dynamics.

KEY WORDS: Infragravity waves; break-point forcing; bound-wave shoaling; shallow foreshores; sea dike; composite modelling; XBeach.

INTRODUCTION

Infragravity waves (IG), also referred to as "long", "surfbeat" or "tsunami-like" waves, are now widely recognized as significant contributors to critical nearshore processes. These often-hazardous processes include: beach and dune erosion (Roelvink *et al.*, 2009); the development of seiches in harbours (Okihiro *et al.*, 1993); and wave-driven coastal inundation (Stockdon *et al.*, 2006). Among recent cases are: at the rocky coast of Banneg island, where unexpectedly high run-up levels were observed (Sheremet *et al.*, 2014); during Typhoon Haiyan, where extensive damage and casualties occurred along a coral-reef-lined coast in the Philippines (Roeber and Bricker, 2015; Shimozono *et al.*, 2015); and on the west coast of France, where several dunes were eroded and "over-washed" (Baumann *et al.*, 2017). In each of these cases, the observed extreme water levels and resulting damage have been attributed to the presence or dominance of nearshore IG waves. Despite this, many of the widely-used empirical and numerical models either only indirectly consider IG-wave dynamics (e.g. EurOTop empirical models) or neglect them completely (e.g. SWAN numerical model). This leads to significant uncertainty in the applicability of these models in environments where IG waves dominate over wave motions at higher frequencies, that is, those typically referred to as sea and swell (SS).

In the ocean, these long-period, low-amplitude waves are formed through nonlinear interactions of SS-wave components (Longuet-Higgins and Stewart, 1962). The resulting wave-group pattern, with sequences of higher and lower amplitudes, generates an IG wave which travels phase-locked or "bound" to the wave group. As SS waves approach shallow water, they may experience shoaling over gently-sloping foreshores and continue to transfer energy to the bound IG wave resulting in amplitude growth. After SS waves break, the wave-group structure disappears and the bound IG wave is freed (released) (Masselink, 1995). Alternatively, IG waves may be generated on steeply-sloping foreshore slopes by the temporal variation in the location of breaking waves. This occurs when alternating groups of higher and lower amplitude wave groups break farther and closer to the shore, respectively. The resulting fluctuations in wave set-up and set-down, with the period of the wave groups, produce both seaward and shoreward propagating IG waves (Symonds *et al.*, 1982; Battjes *et al.*, 2004). These free IG waves propagate in very shallow water where they either slowly dissipate by: i) bottom friction (Henderson and Bowen, 2002; Pomeroy *et al.*, 2012), ii) IG-wave breaking (Van Dongeren *et al.*, 2007; de Bakker *et al.*, 2014), iii) the nonlinear transfer of energy back to higher frequencies (Henderson *et al.*, 2006); or are reflected off the coast or structure leading to (partially) standing waves (Sheremet *et al.*, 2002).

In general it is understood that SS-wave breaking results in a decrease in energy at higher frequencies towards the shore (as the water depth becomes shallower); while the energy at IG frequencies can be substantial and may even exceed that at SS frequencies (Guza and Thornton, 1985; Schäffer, 1993). In the present study, we investigate the factors that contribute to the growth and dominance of IG waves at the dike toe. In particular, we focus on very and extremely shallow conditions; where the ratio of water depth at the dike toe to offshore significant wave height (relative water depth), $\hat{h} = h_{toe}/H_{m0} < 1$.

METHODS

Physical Model Description

The physical modelling was conducted at Flanders Hydraulics Research in a 70-m long, 4-m wide and 1.45-m deep wave flume (Altomare *et al.*, 2016). The experiments simulated wave transformation over a smooth 1:50 foreshore slope (α_{fore}) backed by a 1:2 sloping dike (Figure 1) with varying offshore significant wave heights (H_{m0}), spectral peak periods (T_p) and initial still-water depths at dike (h_{toe}). The flume, equipped with active reflection compensation and second-order wave generation, produced irregular waves which corresponded to a JONSWAP-type spectrum with a peak enhancement factor of 3.3 with a duration approximately equal to 1000 times T_p (~1000 waves). The variations of water-surface elevations were measured using 10 resistance-type gauges, all synchronously sampling at 50 Hz (Figure 1). Considering a geometric scaling of 1:25, the dike toe is taken as 1 m seaward of the dike base in prototype scale (at gauge 10). A summary of the test conditions is provided in Table 1.

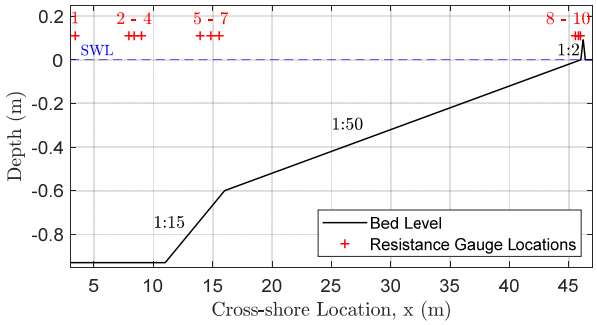

Figure 1. Physical model setup showing resistance gauge locations.

Table 1. Summary of test conditions with relative water depth ($\hat{h}$) normalized bed-slope (β_b, Equation 7) and relative infragravity wave energy ($\widetilde{H}_{IG}$, Equation 12) values.

Test No.	H_{m0} (m)	T_p (s)	h_{toe} (m)	$\hat{h}$	β_b	$\widetilde{H}_{IG}$
1	0.067	2.30	0.030	0.448	0.50	1.05
2	0.057	2.53	0.001	0.018	0.53	1.43
3	0.085	2.32	0.001	0.012	0.47	1.74
4	0.100	2.32	0.001	0.010	0.48	1.82
5	0.121	2.30	0.001	0.008	0.42	2.01
6	0.068	2.28	0.050	0.735	0.41	0.85
7	0.059	2.48	0.051	0.847	0.48	0.70
8	0.065	2.28	0.050	0.769	0.48	0.82
9	0.114	2.31	0.050	0.439	0.41	1.20
10	0.115	2.53	0.050	0.435	0.42	1.12
11	0.060	2.29	0.032	0.517	0.49	0.96
12	0.052	2.48	0.002	0.038	0.55	1.39

Numerical Model Description

For this study, we applied the open-source XBeach numerical model (Roelvink *et al.*, 2009). The nonhydrostatic mode (XB-NH) resolves both infragravity and sea-swell wave motions and is thus referred to as phase-resolving. It computes depth-averaged flow due to waves and currents using the non-linear shallow water equations.

The numerical simulations were configured using a 1D approach to represent the actual flume conditions. In the current study, we apply the configuration of Lashley *et al.* (2018) which obtained reasonably accurate results when applied to similar shallow environments (fringing reefs). As such, the maximum breaking wave steepness (*maxbrsteep*) was set to 0.5 compared to its default value of 0.6, allowing wave breaking to initiate slightly sooner; the relatively smooth flume bottom was represented using Manning's roughness coefficient (n) of 0.12 s/m$^{1/3}$—representative of smooth concrete—and a uniform horizontal grid size, Δx of 2.5 cm was applied. No further tuning of the model was done as part of this study. The model was forced with parametric JONSWAP spectra and initial water-levels at the offshore boundary to match those observed during the physical experiments (Table 1). The model simulation times, output locations and output frequencies were also set to match the experimental data.

Validation Metrics

In order to assess the performance of XB-NH, we applied the following objective functions: Scatter Index (SCI, Eq. 1), as a normalized measure of error and Relative Bias ($Rel.bias$, Eq. 2), as an indicator of prediction bias.

$$SCI_{\Psi} = \frac{\sqrt{\frac{1}{n}\sum_{i=1}^{N}\left(\Psi_{XB}^{i}-\Psi_{Obs}^{i}\right)^{2}}}{\frac{1}{n}\sum_{i=1}^{N}\Psi_{Obs}^{i}}, \quad (1)$$

and

$$Rel.bias_{\Psi} = \frac{\sum_{i=1}^{N}\left(\Psi_{XB}^{i}-\Psi_{Obs}^{i}\right)}{\sum_{i=1}^{N}\Psi_{Obs}^{i}}, \quad (2)$$

where Ψ represents the parameter being evaluated; and subscripts XB and Obs refer to XBeach predictions and observations during the physical experiment, respectively.

Data Processing and Analysis

Separation of Sea-swell and Infragravity Waves

Time series of surface elevation, $\eta(t)$, were analysed using the Welch's average periodogram method and a Hann filter with a 50% maximum overlap. The resulting one-dimensional spectra of wave energy density, $C_{\eta\eta}(f)$, had ~43 degrees of freedom and a frequency resolution of ~0.008 Hz. The significant wave height in both the SS ($H_{m0,SS}$) and IG ($H_{m0,IG}$) bands were then determined as follows:

$$H_{m0,SS} = 4\sqrt{\int_{f_p/2}^{1} C_{\eta\eta}\,df}, \quad (3)$$

and

$$H_{m0,IG} = 4\sqrt{\int_{0.005}^{f_p/2} C_{\eta\eta}\,df}, \quad (4)$$

where half the peak frequency ($f_p/2 = 1/(2T_p)$) is taken as the cut-off to separate SS and IG motions (Roelvink and Stive, 1989). This choice of cut-off frequency is based on the tendency that, in deep water, the majority of SS-wave energy is found at frequencies > $f_p/2$ while the majority of IG-wave energy lies at frequencies <$f_p/2$.

Infragravity-wave Generation Mechanism

To investigate the IG-wave generation mechanisms—by either: i) shoaling of the bound wave; or ii) breakpoint forcing—a cross-

correlation analysis was carried out between the envelope of the SS waves, $|A(t)|$ and the low-pass filtered ($< f_p/2$) surface elevation time series , $\eta^{IG}(t)$, which represents IG motions. Following Janssen *et al.* (2003), $|A(t)|$ was calculated as:

$$|A(t)| = |\eta^{SS}(t) + i\Gamma\{\eta^{SS}(t)\}|^{IG}, \quad (5)$$

where $\eta^{SS}(t)$ is the high-pass filtered ($> f_p/2$) surface elevation time series which represents SS motions, and Γ denotes the Hilbert transform operator.

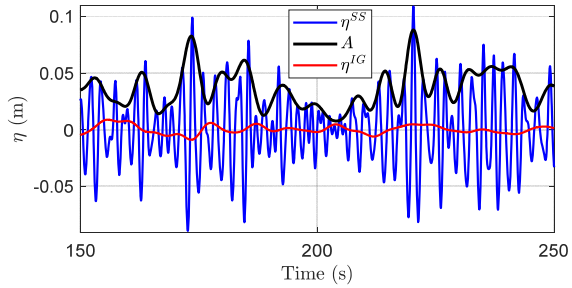

Figure 2. Examples of η^{SS}, η^{IG} and SS-wave envelope (A), obtained using Eq. 5.

The degree of similarity between $A(t)$ (offshore) and $\eta^{IG}(t)$ was then determined using the following cross-correlation function:

$$R_{\eta A} = \frac{\langle \eta^{IG}(t)A(t+\tau)\rangle}{\sigma_\eta \sigma_A}, \quad (6)$$

where $\langle \dots \rangle$ denotes a time averaging operator; τ denotes a time shift; and σ_η and σ_A are the standard deviations of $\eta^{IG}(t)$ and $A(t)$, respectively; and $-1 \leq R_{\eta A} \leq 1$. This approach has been found to successfully identify both incoming (negative $R_{\eta A}$) and outgoing free IG waves (positive/negative $R_{\eta A}$) (e.g. List, 1992; Janssen *et al.*, 2003); incoming break-point generated IG waves (positive $R_{\eta A}$); and outgoing break-point generated IG waves (negative $R_{\eta A}$) (e.g. Baldock and Huntley, 2002; Pomeroy *et al.*, 2012).

Additionally, the relative significance of each generation mechanism for nearshore IG waves may be identified by the normalized bed-slope parameter (β_b), following Battjes *et al.* (2004):

$$\beta_b = \frac{\beta}{\omega}\sqrt{\frac{g}{h_b}}, \quad (7)$$

where β is the bed slope (taken here as $\tan \alpha_{fore}$); the angular frequency of the IG wave, $\omega = 2\pi f_{low}$; f_{low} is the mean frequency of the IG wave; and the mean breaker depth, $h_b = H_{m0}/\gamma$. Here, the ratio of breaking waves to local water depth—the so-called breaker parameter (γ)—is taken as 0.5 (Hofland *et al.*, 2017). Battjes *et al.* (2004) found that for a "mild-slope regime" ($\beta_b \leq 0.3$), the amplitude growth of the IG waves in the shoaling zone is large and breakpoint forcing is ineffective; thus, the bound wave dominates. However, in a "steep-slope regime" ($\beta_b \geq 1$) break-point generated waves are expected to dominate over the weakly-enhanced bound wave.

Separation of Incoming and Outgoing Signals

An additional reflection analysis was carried out by separating the total surface elevation signal into incoming, $\eta_{in}(t)$, and outgoing, $\eta_{out}(t)$, components as follows (Guza *et al.*, 1984):

$$\eta(t) = \eta_{in}(t) + \eta_{out}(t), \quad (8)$$

$$\eta_{in}(t) = \frac{\eta(t) + \sqrt{\frac{h}{g}}u(t)}{2}, \quad (9)$$

and

$$\eta_{out}(t) = \frac{\eta(t) - \sqrt{\frac{h}{g}}u(t)}{2}, \quad (10)$$

where h is the water depth at the location (including wave-induced setup); and $u(t)$ is the signal of horizontal velocities. These signals were then used to calculate the incoming and outgoing significant wave heights in both the SS ($H_{m0,SS,in}$ and $H_{m0,ss,out}$) and IG ($H_{m0,IG,in}$ and $H_{m0,IG,out}$) frequency bands with Eq. 3 and Eq. 4, respectively.

Standing-wave Identification

The frequencies at which nodes in a standing wave occur were predicted as follows (Buckley *et al.*, 2018):

$$f_{node} = \frac{1}{4}(2m-1)\left(\int_x^{x_{dike}} \frac{1}{\sqrt{gh}}dx\right)^{-1}, \quad (11)$$

where x_{dike} is the dike location (point of reflection), m is the number of nodes from the reflection point ($m = 1$ corresponds the fundamental mode of the dike-foreshore system); and x corresponds to the cross-shore position of interest. This equation considers the dike-foreshore system to be an open-ended basin of variable depth.

Infragravity-wave Dominance

Finally, we assessed the relative significance of nearshore IG waves ($\tilde{H}_{IG}$) as the ratio of $H_{m0,IG}$ to $H_{m0,SS}$; and, as we are particularly interested in the local conditions at the toe of the structure, we define IG-wave dominance as:

$$\tilde{H}_{IG} = \frac{H_{m0,IG,toe}}{H_{m0,SS,toe}} > 1. \quad (12)$$

RESULTS AND DISCUSSION

XBeach Validation

Mean Water Levels

The mean water levels ($\bar{\eta}$) predicted by XBeach compare well with those observed during the physical experiment (Figure 1), with minor SCI (0.067) and $Rel.bias$ (0.054) error values.

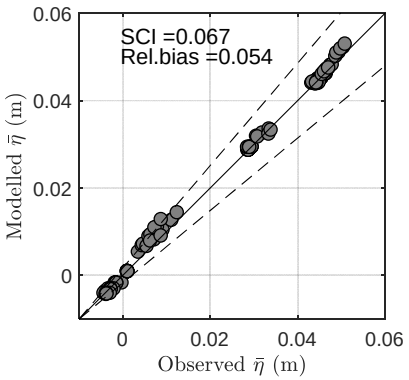

Figure 3. Modelled and observed comparison of $\bar{\eta}$.

In particular, the location and magnitude of the rise in $\bar{\eta}$ near the dike ($x > 45\ m$) is well represented (Figure 4). This increase in $\bar{\eta}$ near the dike, referred to as wave-induced setup, is generated by waves breaking over the shallow foreshore.

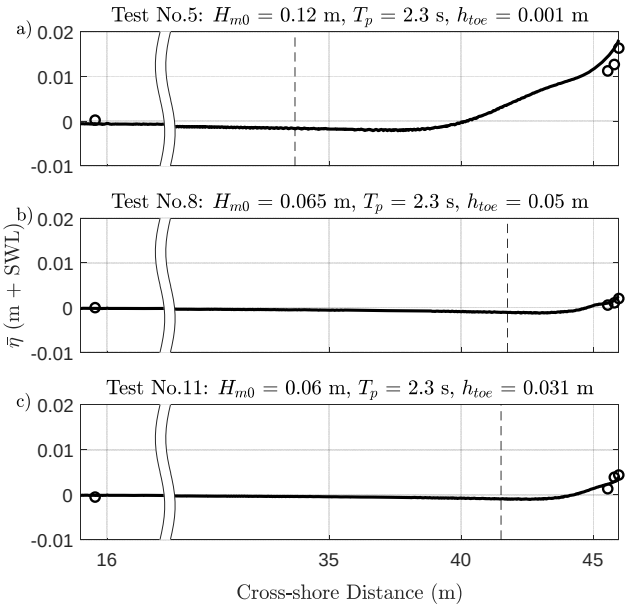

Figure 4. Comparison of modelled (solid lines) and observed (circles) $\bar{\eta}$ for 3 representative tests. Dashed vertical lines indicate mean breakpoint.

Wave Transformation

Figure 5 shows good agreement between the modelled and observed $H_{m0,IG}$ and $H_{m0,SS}$. Both parameters show little bias, $Rel.bias$ values of 0.047 and 0.01, respectively; while $H_{m0,IG}$ predictions—though accurate ($SCI = 0.116$)—show more scatter than predictions of $H_{m0,SS}$ (SCI = 0.05). Cross-shore profiles in Figure 6 show the growth ($x > 30\ m$) of $H_{m0,SS}$ during shoaling and the subsequent dissipation by wave breaking ($x > 40\ m$). Conversely, $H_{m0,IG}$ is enhanced during shoaling but continues to grow as SS waves break, resulting in IG-wave dominance near the dike ($x > 45\ m$). This is also seen in the wave spectra (Figure 7) where the peak in $C_{\eta\eta}(f)$ shifts from SS to IG frequencies from offshore to the dike toe. XBeach accurately captures this, though the offshore peak is somewhat overestimated (Figure 7a, c and e).

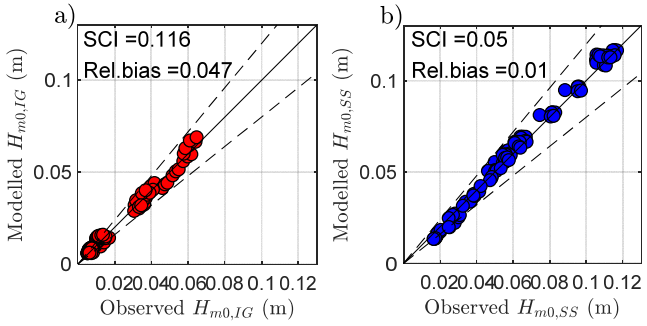

Figure 5. Modelled and observed comparison of a) $H_{m0,IG}$ and b) $H_{m0,SS}$.

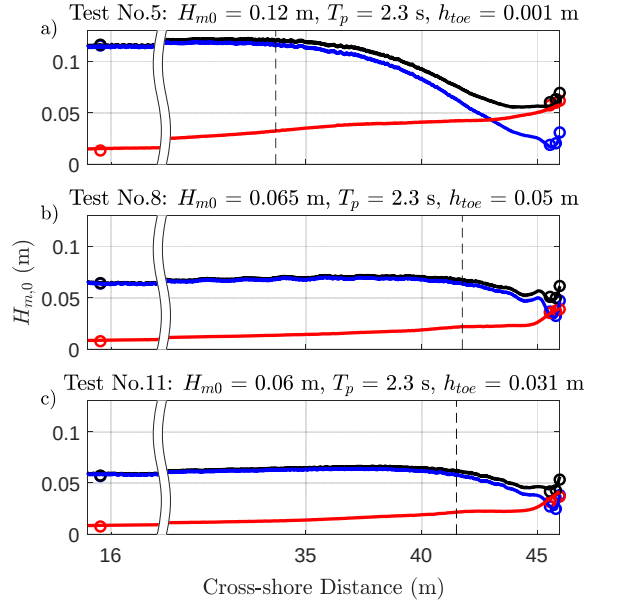

Figure 6. Comparison of modelled (solid lines) and observed (circles) H_{m0} for the SS (blue). IG (red) bands and total (black) signals, for 3 representative tests.

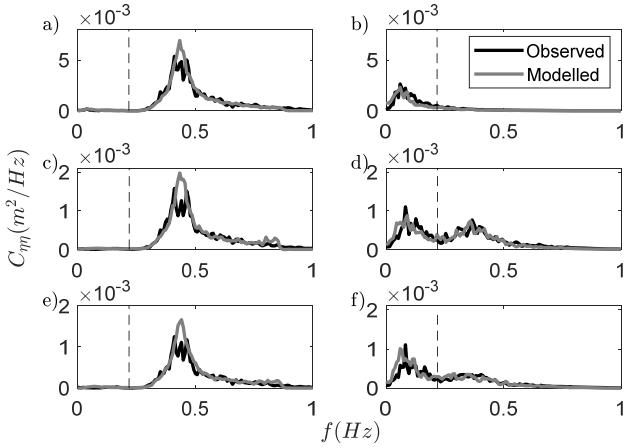

Figure 7. Comparison of modelled and observed wave spectra offshore at gauge 1 (a, c and e) and at the dike toe at gauge 10 (b, d and f) for Tests No. 5 (upper), No. 8 (middle) and No. 11 (lower).

Infragravity-wave Generation Mechanism

Figure 8a shows the cross-correlations between the modelled local $\eta^{IG}(t)$, and $A(t)$ offshore ($x = 0\ m$) for Test No. 11 of the physical experiment, as a representative of the wider observations. The slight negative correlation seen at zero time lag ($\tau = 0\ s$) corresponds to the trough of a bound IG wave that is π radians out of phase with the incident wave groups (Longuet-Higgins and Stewart, 1962).

At $x \sim 10\ m$, both this negative signal and a bar of positive correlation—which represents the crest of the bound wave—becomes more visible. Shoreward of this point ($x > 10\ m$), the positive/negative form of the cross-correlation becomes stronger; this is consistent with an incident bound wave developing an asymmetric form during shoaling (List, 1992; Baldock and Huntley, 2002). Concurrently, the lag between the wave

group—travelling with velocity (c_g), based on *linear wave theory* (black dashed line in Figure 8a)—and the trough of the bound wave increases. This phase shift allows the transfer of energy between the wave group and the bound wave, resulting in IG wave growth (Van Dongeren and Svendsen, 1997).

Shoreward of the breakpoint ($x_b = 41.5\ m$), the ridge of positive correlation is strongly enhanced, suggesting the contribution of an incoming break-point generated IG wave. The now-enhanced IG wave is reflected at the dike ($x = 46\ m,\ \tau{\sim}23\ s$) and propagates to the offshore boundary ($x = 0\ m,\ \tau{\sim}53\ s$) as a free long wave; that is, a wave propagating with celerity equalled to $\sqrt{gh}$ (dashed black and white line in Figure 8a and b).

Theoretically, breakpoint forcing would result in both incoming and outgoing IG waves propagating away from the breakpoint. However, this is not immediately evident in Figure 8a as the outgoing signal is dominated by that reflected at the dike. To investigate this further, the simulation was re-run with the dike removed and the shoreward boundary set to absorbing-generating (weakly-reflective). In the absence of a reflective boundary, a negatively correlated ridge may be seen extending from the breakpoint ($x_b = 41.5\ m,\ \tau{\sim}30\ s$) to offshore ($x = 0\ m,\ \tau{\sim}49\ s$) (Figure 8b). This negative cross-correlation corresponds to a seaward propagating free IG-wave generated by SS-wave breaking (Baldock, 2006; Pomeroy *et al.*, 2012; Contardo and Symonds, 2013). Thus, the incoming IG waves shoreward of the breakpoint ($x > 41.5\ m$, Figure 8a) are the combined result of enhanced bound waves and the shoreward propagating component of breakpoint forced waves. Accordingly, the IG waves propagating seaward (outgoing) are the combined result of the wave reflected at the dike and the wave radiated seaward directly from the breakpoint.

This finding is further supported by the normalized bed-slope parameter analysis where $\beta_b$ranged from 0.41 to 0.55 for the 12 physical model tests (Table 1). These values are over the threshold for bound-wave shoaling as the main generation mechanism ($\beta_b \leq 0.3$) but still under the threshold for break-point forcing to dominate ($\beta_b \geq 1$). This suggests that both generation mechanisms do indeed contribute to $H_{m0,IG,toe}$.

Reflection of Infragravity-waves at the Dike

The cross-shore evolution of the total, incoming and outgoing significant wave heights in both the SS and IG-bands for Test No. 11 are shown in Figure 9a and b, respectively. The incoming IG waves gain energy over the shallow foreshore as SS waves shoal ($x > 28\ m$) and break ($x \geq 41.5\ m$), before finally experiencing near-complete reflection at the dike ($x = 46\ m$, Figure 9b).

The superposition of the incoming and the reflected outgoing IG signals results in a maximum $H_{m0,IG}/H_{m0,IG,in}$ (antinode) at the dike ($x = 0$, Figure 10) and minimum (node) at $x = -0.3L_0$ which may be evidence of a long-period standing wave (Symonds *et al.*, 1982; Klopman and Meer, 1999). This effect is also evident in $H_{m0,SS}/H_{m0,SS,in}$, however only directly in front of the dike with visible nodes at $x = -0.04L_0$and $x = -0.20L_0$; and antinodes at x =0 and $x = -0.11L_0$ (Figure 10). Following reflection, the outgoing waves experience inverse shoaling—also referred to as de-shoaling (Battjes *et al.*, 2004)—where they reduce in amplitude with increasing water depth; that is, as the wave celerity increases (Figure 9a and b).

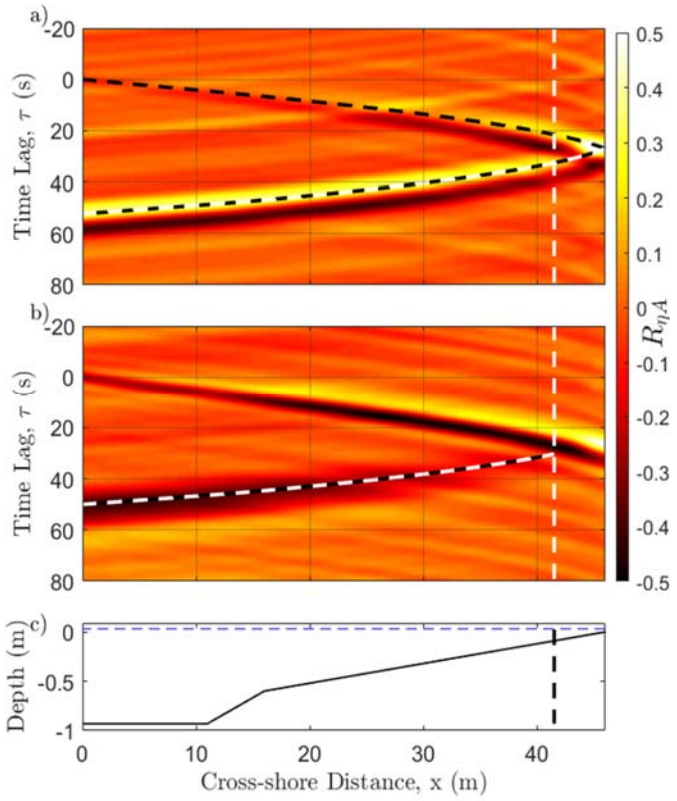

Figure 8 Cross-correlation functions ($R_{\eta A}$) between $A(t)$ at $x = 0$ and $\eta^{IG}(t)$ at all cross-shore locations—as modelled in XBeach—for Test No.11 both (a) with and (b) without the dike. Dashed black lines correspond to an incoming wave group propagating with celerity, c_g; dashed black and white lines represent an outgoing wave propagating with celerity $\sqrt{gh}$. Dashed vertical lines indicate the breakpoint.

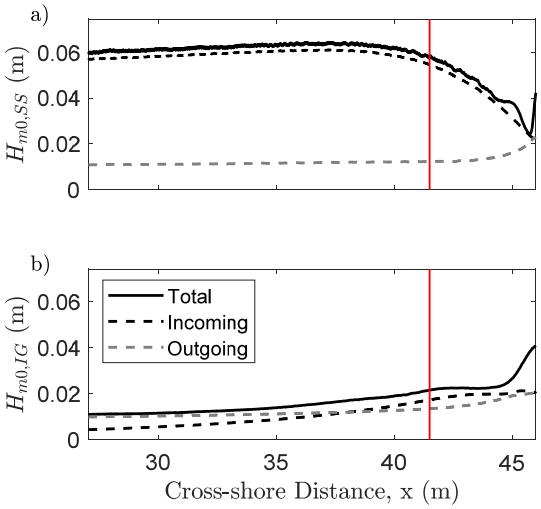

Figure 9 Cross-shore profiles of a) $H_{m0,SS}$ and b) $H_{m0,IG}$ showing total, incoming and outgoing wave heights for Test No. 11. Vertical line indicates mean breakpoint.

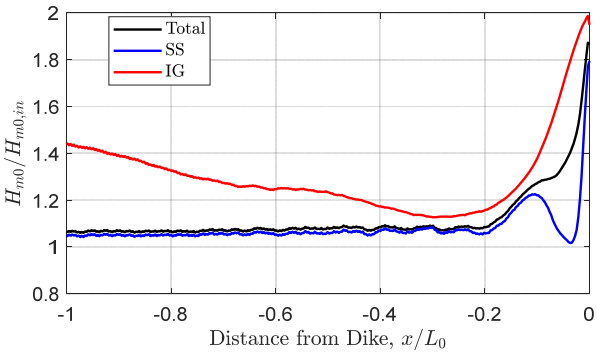

Figure 10. Spatial variation in the ratio of measured to incoming significant wave heights ($H_{m0}/H_{m0,in}$) for the total, SS and IG signals showing nodal/anti-nodal pattern, for Test No. 11.

To investigate the presence of a standing wave, we analyse the evolution of wave spectral density at each cross-shore location, resulting in the spatial plot shown in Figure 11. This was done first considering only the incoming signal (Figure 11a) to exclude the effects of reflection, and then for the total signal where reflection from the dike is included (Figure 11b). A pattern of curved spectral ridges and troughs is clearly visible at low frequencies in Figure 11b but absent in Figure 11a. These locations of minimum and maximum $C_{\eta\eta}(f)$ correspond to nodes and antinodes in a standing wave, respectively (Buckley *et al.*, 2018). This is further corroborated using Eq. 11, as the predicted f_{node} line corresponds well with the minima in $C_{\eta\eta}(f)$.

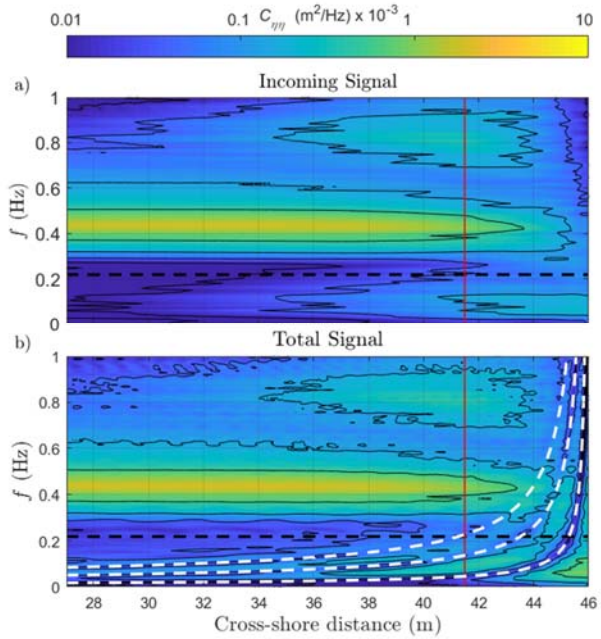

Figure 11. Spatial evolution of wave spectral density for Test No. 11 based on a) the incoming and b) the total surface elevation signals. Dashed white curves show the predicted standing wave nodes (f_{node}, Eq. 11 for m = 1, 2 and 3). Dashed black line shows cut-off frequency separating SS and IG motions. Red line indicates break-point location.

Infragravity-wave Dominance

For the physical model, 8 of the 12 tests showed IG wave dominance ($\widetilde{H}_{IG} > 1$; Table 1). We investigate the dependence of $\widetilde{H}_{IG}$ on three non-dimensional parameters: deep-water wave steepness ($s_0 = (2\pi H_{m0})/(gT_p^2)$), relative water depth ($\hat{h}$) and normalised bed slope (β_b). As can be seen from Figure 12a, $\widetilde{H}_{IG}$ shows a positive linear relationship with s_0; however, with considerable spread suggesting a weak correlation (coefficient of determination, $R^2 = 0.21$).

On the other hand, a strong negative correlation is observed between $\widetilde{H}_{IG}$ and $\hat{h}$ ($R^2 = 0.84$); that is, $\widetilde{H}_{IG}$ is shown to increase as the water depth becomes shallower (Figure 12b). On closer inspection, this trend appears linear for very shallow condition ($0.3 < \hat{h} < 1$) but increases exponentially for the extremely shallow condition ($\hat{h} < 0.3$). This observation is in line with the findings of Hofland *et al.* (2017) who showed that the spectral period ($T_{m-1,0}$) at the dike toe—which can be also seen as a measure of the relative contribution of IG waves—increased exponentially with shallower water depths.

It should also be noted that $\widetilde{H}_{IG}$ showed no dependence on the normalized bed-slope parameter β_b (Figure 12c). However, this was to be expected since the foreshore slope was kept constant ($\cot\alpha_{fore} = 50$) for entire physical experiment.

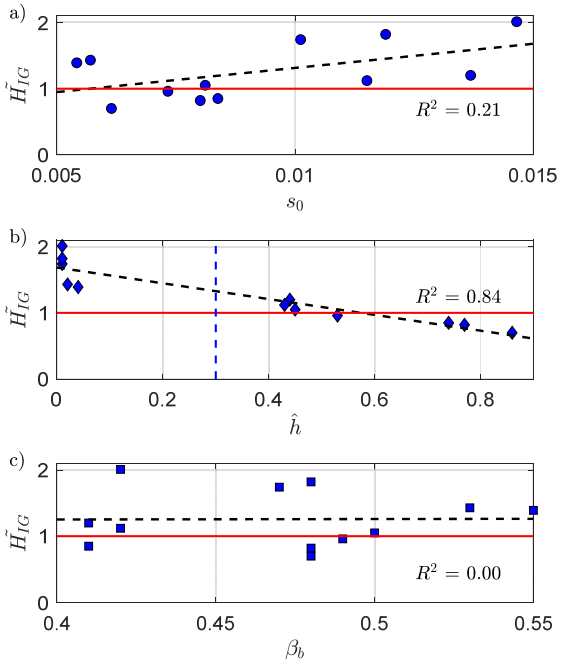

Figure 12. Observed $\widetilde{H}_{IG}$ as a function of a) s_0, b) $\hat{h}$ and c) β_b for the 12 physical model tests. Horizontal lines indicate threshold value for IG wave dominance/non-dominance ($\widetilde{H}_{IG} = 1$). Dashed vertical line in panel 'b' indicates the transition between very ($1 > \hat{h} > 0.3$) and extremely shallow conditions ($\hat{h} < 0.3$).

CONCLUSIONS

A combination of physical and numerical modelling was carried out to investigate the factors that contribute to the growth of nearshore IG waves. Findings show that IG-wave energy at the dike toe is the combined result of bound-wave shoaling and free IG waves generated at the breakpoint. Similarly, the interference of the incoming IG wave and that reflected from the dike forms a standing-wave pattern with a minimum amplitude in the surf zone and a maximum at the shoreline; and thus, gives rise to higher IG-wave heights at the dike toe.

IG-wave dominance is defined, here, as the condition where the relative significance of nearshore IG-wave energy ($\widetilde{H}_{IG}$)—the local ratio of IG to SS wave energy—exceeds a value of 1. This condition is met for 8 of the 12 tests considered, where $\widetilde{H}_{IG}$ shows a strong dependence on relative water depth: $\widetilde{H}_{IG}$ increases as the water depth becomes shallower. These results advocate the importance of accurately representing the contribution of IG waves in extremely shallow environments as their contribution to the total wave height at the dike toe can be as much as twice that of SS waves.

ACKNOWLEDGEMENTS

This work is part of the Perspectief research programme All-Risk with project number P15-21 B, which is (partly) financed by NWO Domain Applied and Engineering Sciences. The authors also acknowledge Dr. Ap van Dongeren for his review of key sections of this manuscript.

REFERENCES

Altomare, C., Suzuki, T., Chen, X., Verwaest, T. and Kortenhaus, A., 2016. "Wave overtopping of sea dikes with very shallow foreshores". *Coastal Engineering*, 116: 236-257.

Baldock, T., 2006. Long wave generation by the shoaling and breaking of transient wave groups on a beach. Proceedings of the Royal Society of London A: Mathematical, Physical and Engineering Sciences, p.^pp. 1853-1876.

Baldock, T.E. and Huntley, D.A., 2002. "Long-wave forcing by the breaking of random gravity waves on a beach". *Proceedings of the Royal Society A: Mathematical, Physical and Engineering Sciences*, 458(2025): 2177-2201.

Battjes, J.A., Bakkenes, H.J., Janssen, T.T. and van Dongeren, A.R., 2004. "Shoaling of subharmonic gravity waves". *J Geophys Res-Oceans*, 109(C2).

Baumann, J. et al., 2017. "Importance of infragravity waves for the generation of washover deposits". *Marine Geology*, 391: 20-35.

Buckley, M.L., Lowe, R.J., Hansen, J.E., van Dongeren, A.R. and Storlazzi, C.D., 2018. "Mechanisms of wave-driven water level variability on reef-fringed coastlines". *Journal of Geophysical Research: Oceans*, 123(5): 3811-3831.

Contardo, S. and Symonds, G., 2013. "Infragravity response to variable wave forcing in the nearshore". *Journal of Geophysical Research: Oceans*, 118(12): 7095-7106.

de Bakker, A.T.M., Tissier, M.F.S. and Ruessink, B.G., 2014. "Shoreline dissipation of infragravity waves". *Continental Shelf Research*, 72(Supplement C): 73-82.

Guza, R., Thornton, E. and Holman, R., 1984. Swash on steep and shallow beaches, Coastal engineering 1984, pp. 708-723.

Guza, R.T. and Thornton, E.B., 1985. "Observations of surf beat". *Journal of Geophysical Research: Oceans (1978–2012)*, 90(C2): 3161-3172.

Henderson, S.M. and Bowen, A.J., 2002. "Observations of surf beat forcing and dissipation". *Journal of Geophysical Research: Oceans*, 107(C11): 14-1-14-10.

Henderson, S.M., Guza, R.T., Elgar, S., Herbers, T.H.C. and Bowen, A.J., 2006. "Nonlinear generation and loss of infragravity wave energy". *Journal of Geophysical Research: Oceans*, 111(C12): n/a-n/a.

Hofland, B., Chen, X., Altomare, C. and Oosterlo, P., 2017. "Prediction formula for the spectral wave period tm-1,0 on mildly sloping shallow foreshores". *Coastal Engineering*, 123(Supplement C): 21-28.

Janssen, T.T., Battjes, J.A. and van Dongeren, A.R., 2003. "Long waves induced by short-wave groups over a sloping bottom". *Journal of Geophysical Research: Oceans*, 108(C8).

Klopman, G. and Meer, J.W.v.d., 1999. "Random wave measurements in front of reflective structures". *Journal of Waterway, Port, Coastal, and Ocean Engineering*, 125(1): 39-45.

Lashley, C.H., Roelvink, D., van Dongeren, A., Buckley, M.L. and Lowe, R.J., 2018. "Nonhydrostatic and surfbeat model predictions of extreme wave run-up in fringing reef environments". *Coastal Engineering*, 137: 11-27.

List, J.H., 1992. "A model for the generation of two-dimensional surf beat". *Journal of Geophysical Research: Oceans*, 97(C4): 5623-5635.

Longuet-Higgins, M.S. and Stewart, R.W., 1962. "Radiation stress and mass transport in gravity waves, with application to 'surf beats'". *Journal of Fluid Mechanics*, 13(4): 481-504.

Masselink, G., 1995. "Group bound long waves as a source of infragravity energy in the surf zone". *Continental Shelf Research*, 15(13): 1525-1547.

Okihiro, M., Guza, R.T. and Seymour, R.J., 1993. "Excitation of seiche observed in a small harbor". *Journal of Geophysical Research: Oceans*, 98(C10): 18201-18211.

Pomeroy, A., Lowe, R., Symonds, G., Van Dongeren, A. and Moore, C., 2012. "The dynamics of infragravity wave transformation over a fringing reef". *J Geophys Res-Oceans*, 117(C11).

Roeber, V. and Bricker, J.D., 2015. "Destructive tsunami-like wave generated by surf beat over a coral reef during typhoon haiyan". *Nature Communications*, 6: 7854.

Roelvink, D. et al., 2009. "Modelling storm impacts on beaches, dunes and barrier islands". *Coastal Engineering*, 56(11-12): 1133-1152.

Roelvink, J.A. and Stive, M.J.F., 1989. "Bar-generating cross-shore flow mechanisms on a beach". *Journal of Geophysical Research: Oceans (1978–2012)*, 94(C4): 4785-4800.

Schäffer, H.A., 1993. "Infragravity waves induced by short-wave groups". *Journal of Fluid Mechanics*, 247: 551-588.

Sheremet, A., Guza, R., Elgar, S. and Herbers, T., 2002. "Observations of nearshore infragravity waves: Seaward and shoreward propagating components". *Journal of Geophysical Research: Oceans*, 107(C8).

Sheremet, A., Staples, T., Ardhuin, F., Suanez, S. and Fichaut, B., 2014. "Observations of large infragravity wave runup at banneg island, france". *Geophysical Research Letters*, 41(3): 976-982.

Shimozono, T. et al., 2015. "Combined infragravity wave and sea-swell runup over fringing reefs by super typhoon haiyan". *J Geophys Res-Oceans*, 120(6): 4463-4486.

Stockdon, H.F., Holman, R.A., Howd, P.A. and Sallenger, A.H., 2006. "Empirical parameterization of setup, swash, and runup". *Coastal Engineering*, 53(7): 573-588.

Symonds, G., Huntley, D.A. and Bowen, A.J., 1982. "Two-dimensional surf beat: Long wave generation by a time-varying breakpoint". *Journal of Geophysical Research: Oceans*, 87(C1): 492-498.

Van Dongeren, A. et al., 2007. "Shoaling and shoreline dissipation of low-frequency waves". *Journal of Geophysical Research: Oceans*, 112(C2): n/a-n/a.

Van Dongeren, A.R. and Svendsen, I.A., 1997. Quasi 3-d modeling of nearshore hydrodynamics, Delaware Univ. Newark Center for App. Coast. Research.